Supplementary Methods

1. Sub-nanometre Localization of individual Fluorescent Probes using Active Feedback Stabilization

Fluorescence photons encode information about the position of the emission source, with a single photon providing a spatial uncertainty of order the wavelength λ[40]. For fluorescence photons collected through the aperture of a microscope objective lens and imaged on a pixelated detector, with pixel size *a* (in units of nm) and background r.m.s. noise in each pixel *b* (number of photon counts), the statistical uncertainty σ in the position of the fluorescence emitter is[41] $\sigma^2 = \frac{s^2 + a^2/12}{N} + \frac{8\pi s^4}{a^2}\frac{b^2}{N^2}$, where *s* (in nm) is the standard deviation of the image Point-Spread-Function and *N* is the total number of collected photons. The pixelation noise assumes a top-hat distribution of size *a* and is valid when $s > a$[41].

For the measurements of Cy3 and Cy5 attached to a short DNA duplex, the pixel size is a=64nm, while the standard deviation of the Cy3 image is actively locked with the 3D piezoelectric stage at s_{Cy3}=2.05pxls=131.2nm, ensuring that each molecule is reproducibly imaged at a well-defined focal plane. With the Cy3 locked, s_{Cy5}=2.45pxls=156.8nm for the Cy5 image (Supplementary Figure 3A). In each CCD exposure we collect N_{Cy3}=3470±260 and N_{Cy5}=11925±1145 photons from Cy3 and Cy5 respectively, while the background photon noise from auto-fluorescence in each pixel is b^2_{Cy3}=6±1 and b^2_{Cy5}=26±3 (photons)^2. Based on the number of photons and the total background noise $b^2_{Cy3,Cy5}$+ b^2_0, including CCD readout noise equivalent to b^2_0=27 (photons)^2, typical precision attained from each CCD exposure is σ_{Cy3}=3.20 nm and σ_{Cy5}=1.87 nm (Supplementary Figure 3C). Our active feedback system keeps the molecules locked in the desired *xy* position for *N*=10-100 frames, until photobleaching occurs (Supplementary Figure 3D), allowing collecting $N_{Cy3}^{Total} \approx 1.7\times10^5$ and

N_{Cy5}^{Total}≈5.5×10^5 total photons from each single Cy3 and Cy5 molecule (Supplementary Figure 3E) and reducing the statistical noise to σ_{Cy3}=0.63±0.33 nm and σ_{Cy5}=0.38±0.19 nm respectively (Supplementary Figure 3F).

Similarly, for the measurements of Cy3 and A647 attached to the ~1.6kb optically manipulated DNA constructs, in each CCD exposure s_{Cy3}=2.1pxls=134.4nm, s_{A647}=2.3pxls=147.2nm, N_{Cy3}=3430±350 photons, N_{A647}=10155±385 photons, b^2_{Cy3}=10±0.6 (photons)^2 and b^2_{A647}=21±1 (photons)^2, giving σ_{Cy3}=4.31 nm and σ_{A647}=2.28 nm (Supplementary Figure 4C). The Cy3 is kept locked in the desired position for N~17 frames with the trap ON, until photobleaching occurs (Supplementary Figure 4D), allowing collecting N_{Cy3}^{Total} ≈0.6×10^5 and N_{A647}^{Total}≈1.6×10^5 total photons from each single Cy3 and Alexa647 molecule (Supplementary Figure 4E) and reducing the statistical noise to σ_{Cy3}=1.07±0.38 nm and σ_{A647}=0.46±0.15 nm respectively (Supplementary Figure 4F). Our actual measurements of the Cy3-Alexa647 distances (σ≈1.3nm for 9 frame averaging from each molecule) show that the statistical photon noise accounts for the main error in measurements on a molecule-by-molecule basis, while the active feedback control system is not introducing any apparent additional noise and the optical trap orients each DNA molecule with sub-nanometre reproducibility.

For the Alexa647 EC5-labeled Ecadherin dimer measurements, s_{A647}=2.03pxls=129.9nm, while in each CCD exposure we collect $N_{A647;pre}$=13945±6895 and $N_{A647;post}$=6980±3510 photons before and after the first Alexa647 dye irreversibly bleaches. The background is b^2_{A647}~48±24 (photons)^2, giving $\sigma_{A647;pre}$=1.7 nm and $\sigma_{A647;post}$=2.6 nm (Supplementary Figure 5C). The two dyes were typically imaged for N_{pre}~30 and N_{post}~80 frames, before and after the 1st Alexa647 dye photobleached (Supplementary Figure 5D), allowing collecting $N_{A647;pre}^{Total}$ ≈1.9×10^5 and $N_{A647;post}^{Total}$≈2.7×10^5 total photons (Supplementary Figure 5E) and reducing the

statistical noise to $\sigma_{A647:pre}$=0.63±0.36 nm and $\sigma_{A647:post}$=0.54±0.36 nm respectively (Supplementary Figure 5F).

2. Effect of CCD Photo-Response Non-Uniformity on the localization accuracy

Consider the image of a Gaussian peak with intensity profile given by $I(x) = I_0 e^{-\frac{x^2}{2\sigma^2}}$. The actual image measured by the CCD is $I(x)\cdot(1+\varepsilon(x))$, where $(1+\varepsilon(x))$ is the spatial profile of the CCD Photo-Response Non-Uniformity (PRNU), where variability in conversion of photons to photoelectrons is between different CCD pixels or within a single pixel. The apparent position of the peak is given by the centroid of the image,

$$\langle x\rangle \equiv \frac{\int xI(x)(1+\varepsilon(x))dx}{\int I(x)(1+\varepsilon(x))dx} = \frac{1}{\sqrt{2\pi}\sigma + \int e^{-\frac{x^2}{2\sigma^2}}\varepsilon(x)dx}\int xe^{-\frac{x^2}{2\sigma^2}}(1+\varepsilon(x))dx \cong \frac{1}{\sqrt{2\pi}\sigma}\int xe^{-\frac{x^2}{2\sigma^2}}\varepsilon(x)dx \cdot$$

The peak will be shifted from its initial position due to the PRNU by an amount

$$\delta x(\sigma,\varepsilon) = \langle x\rangle - \langle x\rangle_{\varepsilon=0} \cong \frac{1}{\sqrt{2\pi}\sigma}\int xe^{-\frac{x^2}{2\sigma^2}}\varepsilon(x)dx = \frac{1}{2\pi\sigma}\iint xe^{-\frac{x^2}{2\sigma^2}}e^{-iqx}\tilde{\varepsilon}(q)dqdx \propto \int (q\sigma)e^{-\frac{(q\sigma)^2}{2}}\tilde{\varepsilon}(q)dq \cdot$$

Thus the effect of each Fourier mode $\tilde{\varepsilon}(q)$ of the PRNU on the position of the peak is weighted by the factor $(q\sigma)e^{-\frac{(q\sigma)^2}{2}}$, indicating that the largest deviations are created by inhomogeneities on the PRNU on the scales comparable to the width of the Gaussian peak (Supplementary Figure 6).

The effect of PRNU was tested with the full 2D Gaussian non-linear least-squares fit on simulated images. We created numerically PRNU with variable characteristic length-scales l_0 but fixed standard deviation at 2%. The numerical PRNU maps were generated by starting with a random 128×128 2D array (l_0≡1pixel), filtering it by 2D convolution with a Gaussian kernel of varying width (l_0=1,2,4,8,16,32 pixels) and finally renormalizing to obtain mean=1.0, stdev=0.02. Then we multiply an ideal 2D Gaussian peak of sigma=8 pixels, positioned randomly in the field of view with the

PRNU and fit the resulting image to locate its centre position in x, y. Supplementary Figure 6 shows that the largest deviations in the position are observed for characteristic PRNU length-scale comparable to the width of the 2D Gaussian, in agreement with the analytical calculation.

To access the effect of pixelated read-out, we performed numerical simulations with fixed PRNU length-scale l_0 and PSF size s but varying pixel size a. We started again with a random 128×128 2D array, generating the PRNU map by fixing 4×4 pixel blocks to the same numerical value ($l_0 \equiv 4$pixels). We set the standard deviation of the PRNU map to 1%, 3% and 10% in 3 different runs, and multiplied it with a 2D Gaussian of s=pixels. Subsequently $a \times a$ pixel blocks were summed to generate 2D images with varying pixelation (a=1,2,4,8,16), that were fitted to determine the xy coordinates of the 2D peak. The systematic deviations in xy from the ideal positions depended on the PRNU magnitude and not on the degree of pixelation (Supplementary Figure 7).

3. Experimental Calibration of the inter-pixel CCD PRNU

To calibrate the inter-pixel CCD PRNU we replaced the blue LED used for illuminating the sample in the microscope with a white LED. We imaged a featureless sample on the CCD. Translating the sample in x, y and changing the focus in z did not cause apparent changes on the CCD images. We took 800 images of a region 32×32 pixels with the LED on to measure the response of the CCD, with signal level in each pixel corresponding to ~10^4 photons. We also took 800 images with the LED off to measure the background. The response of each pixel was measured as the average signal minus the average background. Supplementary Figure 8 shows a map of the PRNU. The standard deviation between pixels was about 1.8%.

To calculate the effect of the experimental PRNU on localization and the mapping from the green to the red images we created simulated images of 2D Gaussian peaks with width σ_{green}=2.05pxls and σ_{red}=2.25pxls (corresponding to the measured widths for Cy3 and Cy5). The 2D Gaussian peaks were placed on a 30×30 grid with spacing 0.5pxls, corresponding to the middle 15×15 pixels of the calibrated region. Each 2D Gaussian peak was multiplied by the measured PRNU and fitted with a non-linear least squares algorithm to return its x-y coordinates. Due to the PRNU, there are systematic deviations $\delta\vec{x}^{i} = \left(\vec{x}^{i}_{green,red}, \vec{x}^{i_{grid}}_{green,red}\right)$ of the least-squares fit coordinates $\left\{\vec{x}^{i}_{green}, \vec{x}^{i}_{red}\right\}$ from the perfect grid positions $\left\{\vec{x}^{i_{grid}}_{green}, \vec{x}^{i_{grid}}_{red}\right\}$. For each point $\boldsymbol{i}$ the difference $\delta\vec{x}^{i} = \delta\vec{x}^{i}_{green} - \delta\vec{x}^{i}_{red}$ between the green and red channel corresponds approximately to the non-linear part of the mapping function $\boldsymbol{g}\cdot\boldsymbol{f}^{-1}$ from green to red (since $\boldsymbol{g}\cdot\boldsymbol{f}^{-1}$ is approximately equal to the identity tensor). Supplementary Figure 9 shows spatial maps of δx^{i}, δy^{i} and $\left|\delta\vec{x}^{i}\right|$. The predicted deviation from linearity shows similar spatial features with the experimentally measured non-linearity of fluorescent bead images (Supplementary Figure 9). Thus the inter-pixel CCD PRNU can account for a large part of the ~nanometre deviations on scale of a few pixels observed experimentally. Future work will address whether an inter-pixel PRNU calibration procedure can fully correct the non-linearity in the mapping functions to the sub-nanometre level.

4. Calculation of Systematic Errors when only the mapping between the two colour images is calibrated

Assume two objects are on the sample at positions $\boldsymbol{x}_1$ and $\boldsymbol{x}_2$ and object 1 appears in the green image while object 2 appears on the red image. If one calibrates only the mapping function from green to red images $\boldsymbol{g}\cdot\boldsymbol{f}^{-1}$ and assumes that e.g. $\boldsymbol{g}$ is linear ($\boldsymbol{g}=\boldsymbol{g}_L$ given by only the magnification of the system) then the estimate for the distance between the two objects is $\delta\boldsymbol{x}_L=\boldsymbol{g}_L^{-1}(\boldsymbol{g}\cdot\boldsymbol{f}^{-1}(\boldsymbol{x}_{green})-\boldsymbol{x}_{red})$. In reality $\boldsymbol{g}=\boldsymbol{g}_L+\boldsymbol{g}_{NL}$ with $\boldsymbol{g}_{NL}$ the non-linear part. Thus, the true distance is: $\delta\boldsymbol{x}=\boldsymbol{x}_1-\boldsymbol{x}_2=\boldsymbol{g}^{-1}(\boldsymbol{g}\cdot\boldsymbol{f}^{-1}(\boldsymbol{x}_{green}))-\boldsymbol{g}^{-1}(\boldsymbol{x}_{red})=[\boldsymbol{g}_L^{-}$

$^{1}(\boldsymbol{g}\cdot\boldsymbol{f}^{-1}(\boldsymbol{x}_{\text{green}}))+\boldsymbol{g}_{\text{NL}}^{-1}(\boldsymbol{g}\cdot\boldsymbol{f}^{-1}(\boldsymbol{x}_{\text{green}}))\ ]-[\ \boldsymbol{g}_{\text{L}}^{-1}(\boldsymbol{x}_{\text{red}})+\boldsymbol{g}_{\text{NL}}^{-1}(\boldsymbol{x}_{\text{red}})]$. The error in the distance estimate due to the $\boldsymbol{g}_{\text{NL}}^{-1}$ is $\delta\boldsymbol{x}_{\text{L}}-\delta\boldsymbol{x}=\boldsymbol{g}_{\text{NL}}^{-1}(\boldsymbol{g}\cdot\boldsymbol{f}^{-1}(\boldsymbol{x}_{\text{green}}))-\boldsymbol{g}_{\text{NL}}^{-1}(\boldsymbol{x}_{\text{red}})\neq 0$.

5. Linear mapping calibration using fluorescent beads

We repeated the mapping function $\boldsymbol{g}\cdot\boldsymbol{f}^{-1}$ calibration shown in Figure 2 C/D with 3 different beads. The result for the mapping coefficients is (mean±standard deviation)

$$\begin{pmatrix}\boldsymbol{x}_{\boldsymbol{red}}\\ \boldsymbol{y}_{\boldsymbol{red}}\end{pmatrix}=\begin{pmatrix}1.000\pm0.002 & -0.004\pm0.011\\ -0.036\pm0.006 & 0.953\pm0.013\end{pmatrix}\begin{pmatrix}\boldsymbol{x}_{\boldsymbol{green}}\\ \boldsymbol{y}_{\boldsymbol{green}}\end{pmatrix}+\begin{pmatrix}0.995\pm0.195\\ 1.774\pm0.236\end{pmatrix},$$

showing excellent reproducibility in the linear coefficients but ~0.2 pixels (12nm) systematic errors in the offset terms. To test the performance of this calibration, for each bead we transformed the positions $\boldsymbol{x}_{\text{green}}$ and calculated the mean deviation $\langle\boldsymbol{g}\cdot\boldsymbol{f}^{-1}(\boldsymbol{x}_{\text{green}})-\boldsymbol{x}_{\text{red}}\rangle$. The typical systematic errors due to bead-to-bead variability were 1.1nm in the X-axis and 1.5nm in the Y-axis.

6. Calibration of the mapping function $g\cdot f^{-1}$ using Cy3 and Cy5 attached to 20bp DNA duplex

We used single Cy3 and Cy5 molecules attached at the ends of the 20bp DNA duplex to directly calibrate the mapping functions. One end also contained a biotin moiety and was attached to the streptavidin-coated cover-glass surface. We locked the position $\boldsymbol{x}_{\text{green}}$ of Cy3 and measured the position $\boldsymbol{x}_{\text{red}}$ of the Cy5. The $\boldsymbol{x}_{\text{green}}$ set-point was scanned on 9 separate points arranged on a 3x3 grid, spaced by 0.5 pixels to calibrate a square region of size 1 pixel (Supplementary Figure 16). Since there was variation of ~1.5nm between individual Cy5 molecules, for each grid point we measured N~10 different DNA duplexes to collect enough data for sub-nanometre localization precision. The linear mapping is

$$\begin{pmatrix} x_{red} \\ y_{red} \end{pmatrix} = \begin{pmatrix} 1.002 \pm 0.013 & 0.018 \pm 0.013 \\ -0.058 \pm 0.032 & 0.971 \pm 0.032 \end{pmatrix} \begin{pmatrix} x_{green} \\ y_{green} \end{pmatrix} + \begin{pmatrix} 0.526 \pm 0.004 \\ 1.909 \pm 0.011 \end{pmatrix}.$$

The linear mapping coefficients agree to ~0.02 with the ones obtained with fluorescent beads, while the constant terms have errors 0.005-0.01pxls (0.3-0.6nm). We use this mapping function for measuring Cy3-Cy5 distances.

7. Measurement of the DNA end-to-end extension

During the stretching experiments the position of the microspheres was measured both with the trap on and off when the Cy3 was locked to estimate an average displacement x_b=762.5±5.5 nm along the stretching axis (Supplementary Figure 11). To estimate the end-to-end distance of the DNA molecule x_{dna} we take into account the size of the microsphere a=250nm as well as the length x_{linker} of the DNA-bead and DNA-surface linkages. The PEG length is about 110 monomers (3400kDa+3400kDa=6800kDa at 62Da/monomer). The end-to-end distance of PEG at ~10pN is ~0.15nm/monomer[42], i.e. the total length contribution from the PEG is 17nm. The size of the anti-digoxigenin antibody is ~10nm but there are uncertainties in its orientation. The size of the carbon-chain linkers between the DNA and the biotin and digoxigenin moieties is ~1nm while the distance of biotin-binding sites on a streptavidin tetramer is ~2-3nm. Thus the total linkage length is ~30nm, with uncertainties ~5-10nm due to the unknown orientation of the antibody and the streptavidin orientation as well as potential polydispersity of the PEG chains. The end-to-end distance is given by $x_{dna}=(a^2+x_b^2)^{1/2}-(a+x_{link})\approx 522$nm with a total error of 11 nm obtained by combining the measurement error in x_b, the uncertainty in x_{link} and the variability in bead radius a (5.7nm based on 2.3% CV specifications from the manufacturer). The extension of the DNA for contour length 540nm then is 96.7(±2)%.

8. Estimation of the statistical error for each Cy3-A647 distance measurement

The statistical error for each Cy3-A647 distance measurement is estimated as $\text{error} = \frac{\text{sigma}}{\sqrt{N_{total} / N_{average}}}$, where sigma is the standard deviation of each Gaussian peak, N_{total} is the total counts in each peak and $N_{average} \equiv 9$ is the number of consecutive frames box-car averaged in each trace.

9. Axial stabilization of the microscope focus

To achieve sub-nanometer registration of the two colour images we perform all calibrations and measurements at a well defined focal plane, since off-axis aberrations and misalignment of the optical components manifest as an axial tilt of the PSF centroid that can vary along the field-of-view and between CCD colour channels. The standard deviation *s* of the PSF increases as a molecule is moving out of focus, so we could reproducibly place individual molecules at a well-defined axial position *z* using our feedback approach by adjusting in real-time the vertical position of the sample with the 3D piezoelectric stage to lock the parameter *s* of the image of the molecule on the CCD. Since d*s*/d*z* varies with *z*, vanishing at the tightest focus, the working setpoint *s* is slightly out of focus to ensure adequate axial sensitivity (~0.1nm/nm). The molecule-to-molecule reproducibility in *s* was ~0.04 pxls=2.5nm (Supplementary Figure 3-4), corresponding to ~25nm in *z*.

Similarly, for the Alexa647-Alexa647 distance measurements, the *x*,*y* and *s* for the image of a 0.5μm bead served as a reference to stabilize the microscope both in *xy* and in *z*. Alternatively, for the *z* stabilization only, a laser beam that is total-internally reflected from the sample is projected onto a position-sensitive-photodetector, giving a signal proportional to the coverslip-objective separation. This second approach has the advantage that the focus stability does not depend on the sharpness of the fiducial image and can be used in non-ideal conditions e.g. when imaging molecules in a cell, however it is very sensitive to the long-term pointing stability of the reference laser beam. In our

set-up using a fiber-coupled laser beam (either the excitation beam or a dedicated NIR pigtailed diode) and by enclosing the microscope to minimize air current and temperature change perturbations, we achieve 3nm axial stability over ~30 minutes time scale (Supplementary Figure 13).

Supplementary Discussion

Improvement in the resolution of wide-field sub-diffraction imaging.

Modern sub-diffraction imaging techniques that are based on stochastic switching and localization of individual fluorescent molecules (e.g. PALM/STORM, PALMIRA, dSTORM, SMACM etc.) feature an effective microscope Point-Spread-Function in the shape of a 2D Gaussian peak with r.m.s. size *s* equal to the uncertainty in the position of each detected molecule. Even though the total photon-count in each switching cycle can be up to several 1000's, in principle allowing localization precision *s* down to the few nanometre range, the current technological state-of-the-art is limited by systematic effects and drift of the apparatus to localization precision *s*~10nm, achieving a final FWHM resolution in the reconstructed image of $\boldsymbol{d} = 2\sqrt{2\ln 2}\boldsymbol{s} = 2.35...\boldsymbol{s}$ ~20nm.

In this paper we present a methodology to reduce the total uncertainty in co-localizing individual fluorescent molecules to *s*<1nm that is readily applicable to improve these existing methods. The active stabilization approach we present can eliminate instrumental drift during data acquisition that is now instead being subtracted during post-processing. In addition to facilitate two-colour imaging of extended structures, the entire field can be broken up into a tilling array of smaller domains where the mapping discussed in this paper is applied. Each domain can be corrected by imaging a micro-fabricated array or a random pattern of individual fluorescent probes and measuring the displacement of each feature of the array feature while the sample is

moved in a known pattern with the piezo-electric stage (or any other precision position encoder).

With the technological improvements we present in this paper the resolution d=2.35s of the current state-of-the art methods can be pushed at the present photon-noise limit of <10nm FWHM. More important, the development of specialized probes that can provide several 10,000's of collected photons in each switching cycle would make full-use of the capability of the technology in this paper to localize each individual molecule with absolute accuracy of s<1nm, allowing resolving densely labelled biological structures with an all-optical FWHM resolution of d≈2nm (or better).

Supplementary Tables

Supplementary Table 1 Fitting parameters for Cy3-A647 distance distributions (Figure 3B in main text).

Cy3-A647 spacing (bp)	Peak Position (nm)	Deviation from Linearity (nm)	Sigma (nm)	N_{total}	Error (nm)	Total Cy3 photons[a] ($\times 10^6$)	Total Alexa647 photons[b] ($\times 10^6$)
0	0	0	2.67	395	0.40	1.35	4.01
105	32.10	-1.185	1.32	233	0.26	0.80	2.37
115	36.39	-0.065	1.3	86	0.42	0.29	0.87
125	39.85	0.225	1.17	251	0.22	0.86	2.55
145	46.59	0.615	1.79	62	0.68	0.21	0.63

[a,b]Total number of photons estimated as N_{total}×3430 and N_{total}×10155 for Cy3 and A647 respectively.

Supplementary Table 2 Fitting parameters for Alexa647-Alexa647 distance distributions (Figure 4C in main text).

Peak position (nm)	Error (nm)	Sigma (nm)	Error (nm)	Area	Error	Total A647 photons[a] pre-bleach ($\times 10^6$)	Total A647 photons[b] post-bleach ($\times 10^6$)
32.25	0.6	3.0	0.6	75.	12.8	14.3	20.3
24.65	1.3	4.4	1.8	46.3	12.3	8.8	12.5
5.25	0.5	2.7	0.6	24.3	4.2	4.6	6.6

[a,b]Total number of A647 photons estimated as $Area \times 1.9 \times 10^5$ and $Area \times 2.7 \times 10^5$ for pre- and post-bleaching respectively.

Supplementrary Table 3 Fitting parameters for main EC5-EC5 distance peak vs. [Ca^{++}] (Supplementary Figure 12).

[Ca^{++}]	Peak Position (nm)	Error (nm)	Sigma (nm)	Error (nm)	Area	Error
3μM	17.95	0.55	6.88	0.60	90.8	6.5
10μM	19.11	0.37	3.05	0.38	56.7	6.0
30μM	21.80	0.54	3.32	0.54	56.4	8.0
100μM	26.99	0.42	3.12	0.43	102.7	12.0

Supplementary References

40. Heisenberg, W., The Physical Principles of the Quantum Theory, Dover Publications, Inc. (1949).

41. Thompson, R.E., Larson, D.R. & Webb W.W., Precise Nanometer Localization Analysis for Individual Fluorescent Probes. *Biophys. J.* **82**, 2775-2783 (2002).

42. Oesterhelt, F., Rief, M. & Gaub**,** H. E. Single molecule force spectroscopy by AFM indicates helical structure of poly(ethylene-glycol) in water. *New J. Phys.* **1**, 6.1-6.11 (1999).

43. Norman, D. et al. Location of Cyanine-3 on Double-Stranded DNA: Importance for Fluorescence Resonance Energy Transfer Studies. *Biochemistry* **39**, 6317-6324(2000).

44. Dickson, R.M., Norris, D.J. & Moerner, W.E. Simultaneous Imaging of Individual Molecules Aligned Both Parallel and Perpendicular to the Optic Axis. *Phys. Rev. Lett.* **81**, 5322(1998).

45. Bartko, A. & Dickson, R. Imaging Three-Dimensional Single Molecule Orientations. *J. Phys. Chem. B* **103**, 11237-11241(1999).

46. Enderlein, J., Toprak, E. & Selvin, P.R. Polarization effect on position accuracy of fluorophore localization. *Opt. Express* **14**, 8111-8120(2006).

Supplementary Figures and Legends

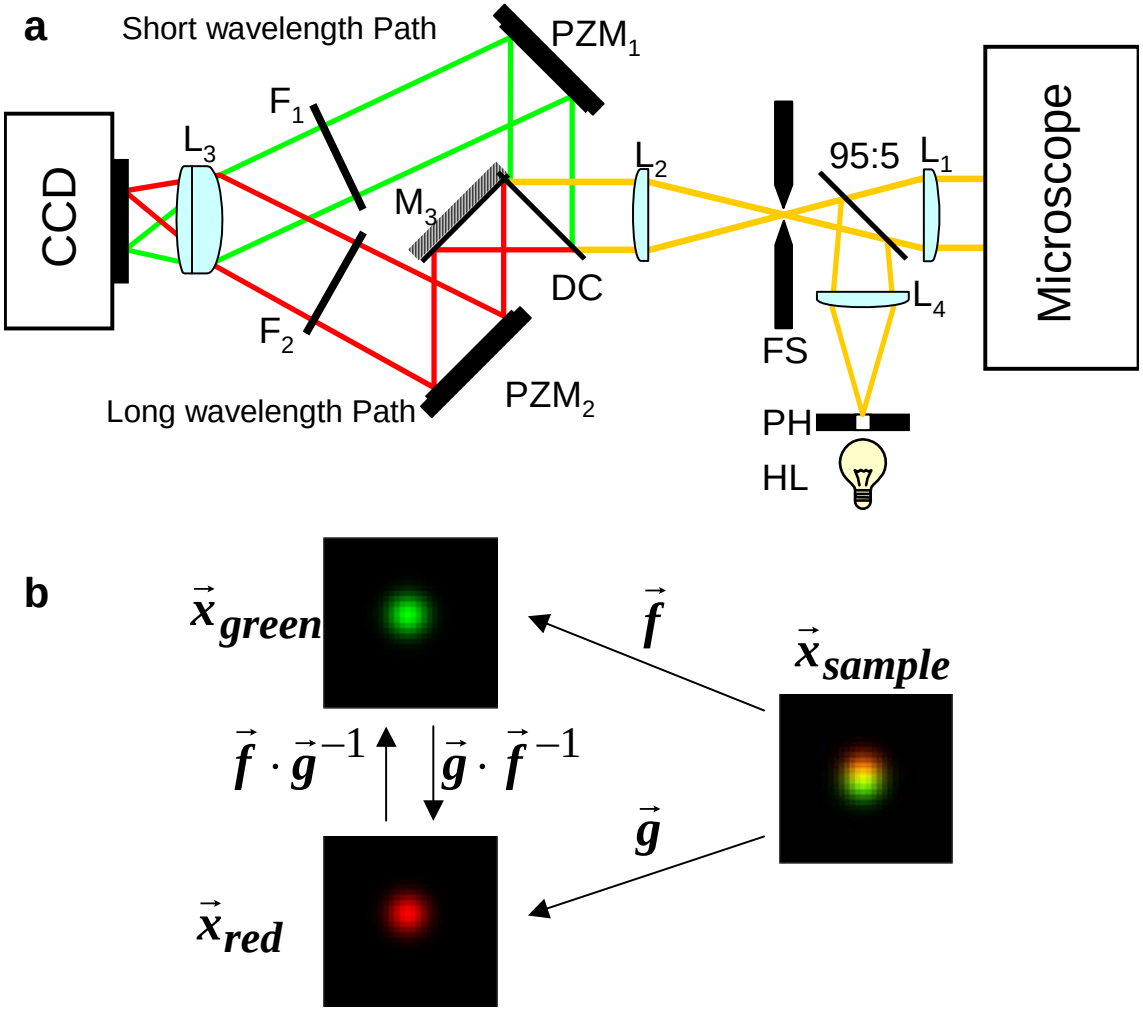

Supplementary Figure 1 Experimental Scheme. (**a**) Optics layout of our two-colour imaging set-up. A relay lens (L_1) projects the image from the microscope to a field-stop (FS) to adjust its size. A pinhole (PH) is illuminated with a halogen lamp (HL) and its image through lens L_4 is combined with the image from the microscope using a 95:5 partially reflective mirror. The light is collimated with lens L_2 and split into green and red colours with a dichroic mirror (DC). The separate colours are projected onto separate regions of the same CCD camera using lens L_3 and the position of the two images are finely adjusted with piezo-mirror mounts (PZM_1 and PZM_2). Band-pass filters F_1 and F_2 select for desired fluorescence wavelengths. M_3 is a fixed mirror. (**b**)

Definition of the mapping functions $\vec{f}$ and $\vec{g}$ that map $\vec{x}_{sample}$ to $\vec{x}_{green}$ and $\vec{x}_{red}$. See Methods Summary for details.

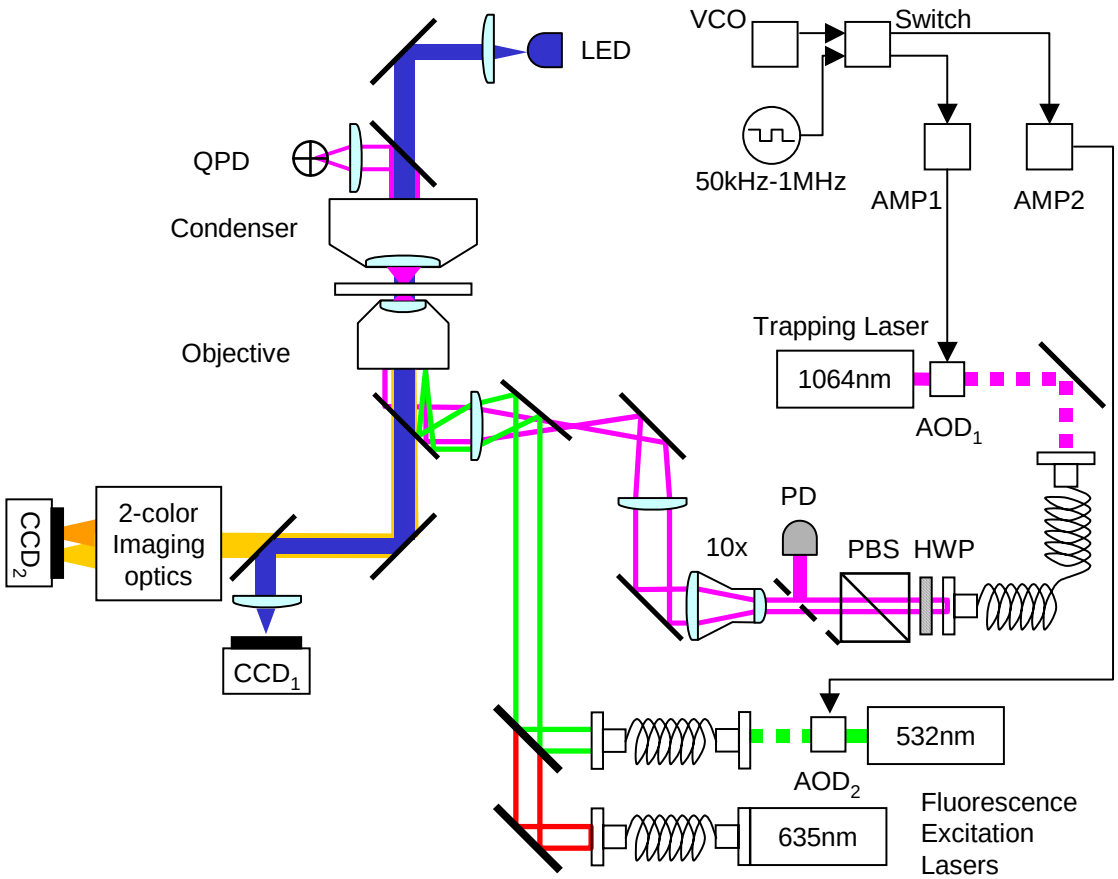

Supplementary Figure 2 Experimental Set-up (described in Methods). All the lasers were delivered to the microscope through single-mode fibres to ensure a clean beam profile and pointing stability. For the 1064nm and the 532nm lasers the 1st order diffracted beams from 2 acousto-optic deflectors (AOD1 and AOD2) were coupled to the fibre. The polarization of the 1064nm beam launched from the fibre was adjusted with a half-wave plate (HWP) and a polarizing beam splitter (PBS). A pick-off mirror and a photo-diode (PD) were used to monitor the intensity of the trapping beam. The trapping beam was expanded 10× to slightly overfill the objective lens back aperture before it was delivered to the microscope. The forward scattered light from the trapping beam

was collected with a condenser lens and projected on a quadrant photo-detector (QPD) that acted as a high bandwidth (~100kHz) position sensor for the trapped bead. The sample was illuminated with an LED and the bright field image was projected on a CCD (CCD1). Tracking the bead with the CCD allowed larger dynamic range but with reduced bandwidth (~1kHz). Fluorescence of Cy3 and Cy5 was excited in TIR mode by the 532nm and 635nm lasers, collected by the objective and imaged with CCD2. The 2-colour imaging optics set-up for simultaneous imaging of Cy3 and Cy5 is shown in Supplementary Figure 1.

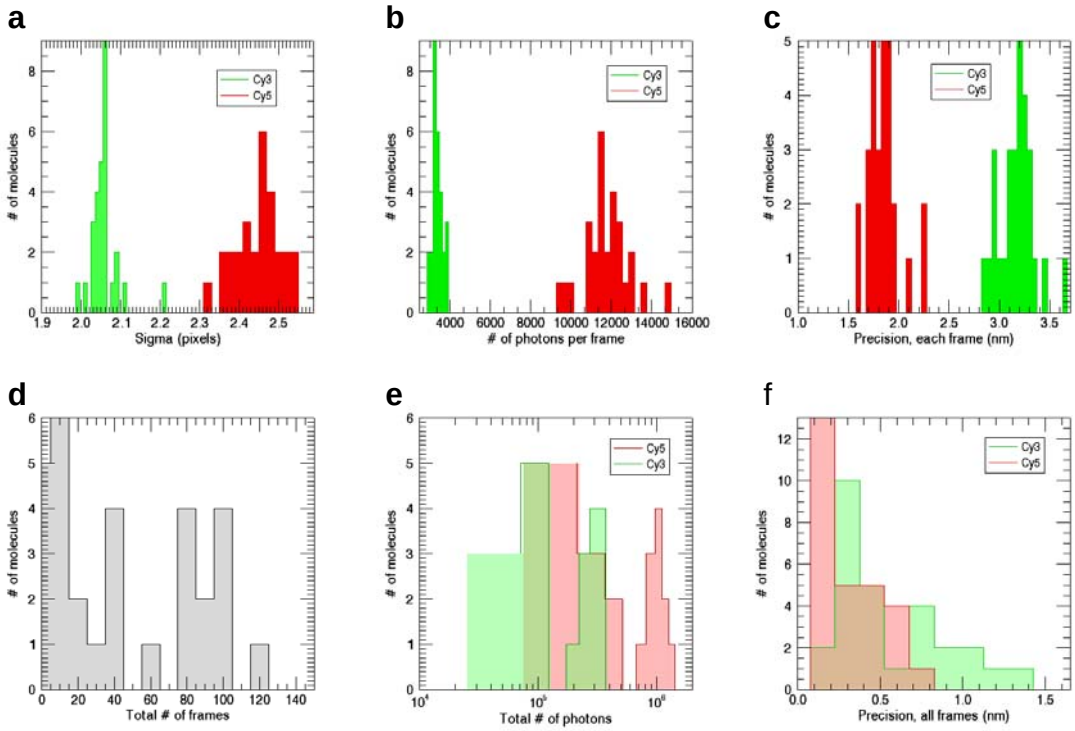

Supplementary Figure 3 Localization of Cy3 and Cy5 on short DNA duplex. The xy position and the PSF sigma of the Cy3 image is actively stabilized by the 3D piezoelectric stage using our real-time feedback system. (**a**) Average PSF standard deviation.(**b**) Average Number of photons collected in each frame. (**c**) Localization precision in each frame. (**d**) Total number of frames that Cy3 is

locked. (**e**) Total number of photons collected. (**f**) Final localization precision from all the frames.

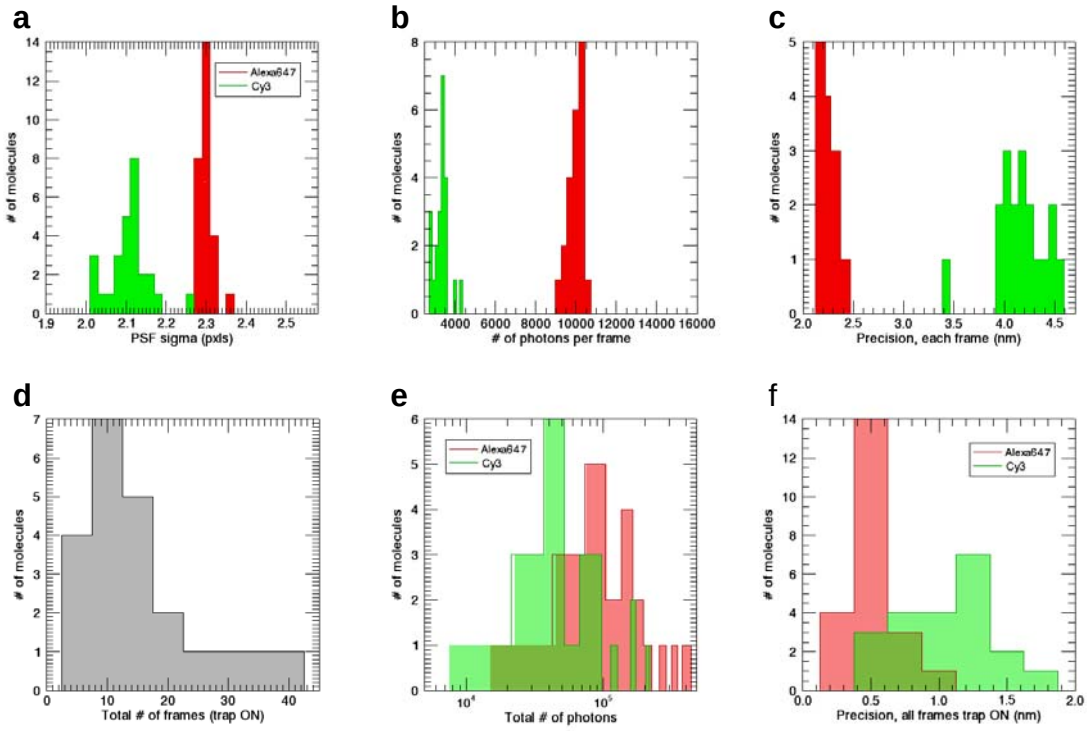

Supplementary Figure 4 Localization of Cy3 and Alexa647 on 1.6kb DNA construct that is manipulated with optical trapping while the Cy3 is actively locked. (**a**) Average PSF standard deviation. (**b**) Average Number of photons collected in each frame. (**c**) Localization precision in each frame. (**d**) Total number of frames that Cy3 is locked. (**e**) Total number of photons collected. (**f**) Final localization precision from all the frames.

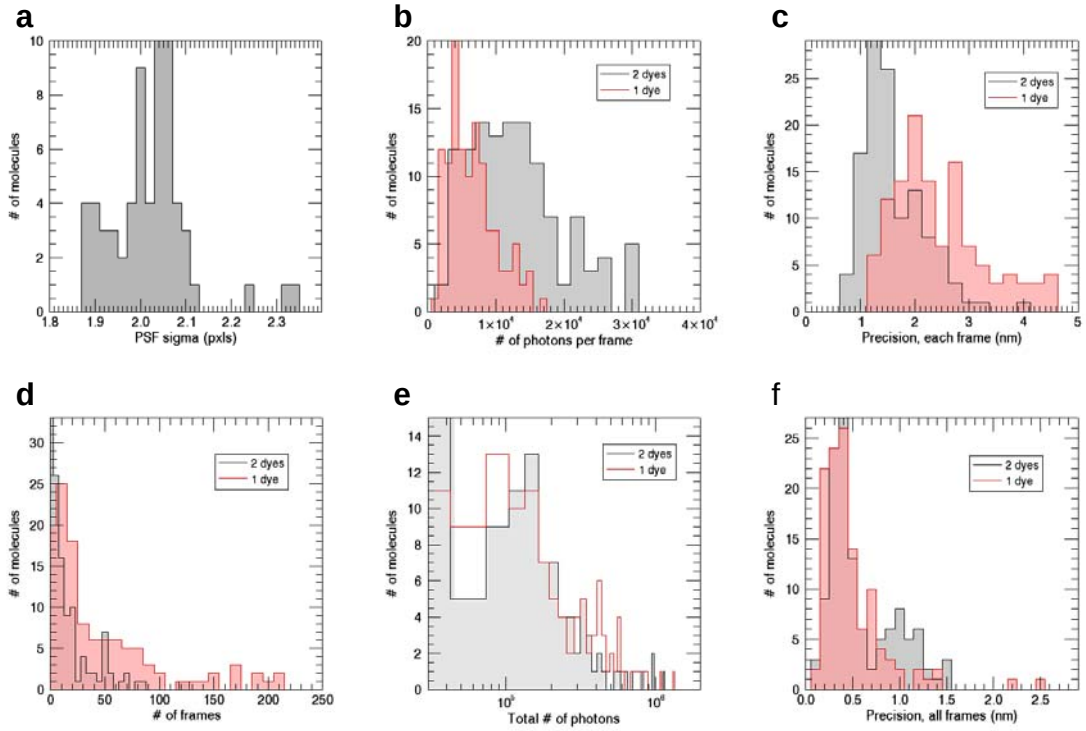

Supplementary Figure 5 Localization of Alexa647 on E-cadherin dimer. The microscope is actively stabilized in 3D using a 0.5μm bead as reference mark in the 2nd colour. (**a**) Average PSF standard deviation in a field of view. (**b**) Average Number of photons collected in each frame. (**c**) Localization precision in each frame. (**d**) Total number of frames before and after the 1st photobleaching step. (**e**) Total number of photons collected. (**f**) Final localization precision from all the frames. The majority of molecules can be tracked before and after photobleaching to ~0.5nm (with a smaller sub-population in the grey histogram that yielded statistical errors ~1nm before the 1st dye bleached).

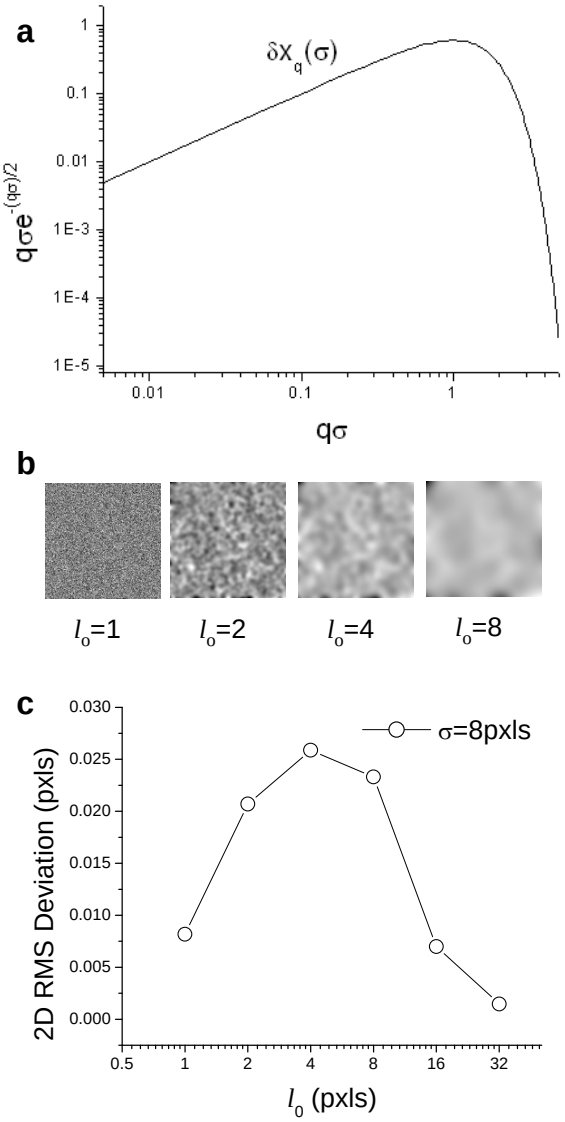

Supplementary Figure 6 Effect of CCD PRNU on Localization Accuracy. (**a**) The weighting factor $(q\sigma)e^{-\frac{(q\sigma)^2}{2}}$ for the contribution of each spatial mode of the PRNU. (**b**) Simulated PRNU with variable characteristic length scale l_0. Simulations were performed for image size 128×128 pixels. (**c**) RMS deviation of the position of a 2D Gaussian peak with width σ=8 pixels vs. l_0. The largest deviation is seen at $l_0 \approx \sigma/2$. Each symbol is the average of N=100 points randomly distributed in the 128×128 ROI.

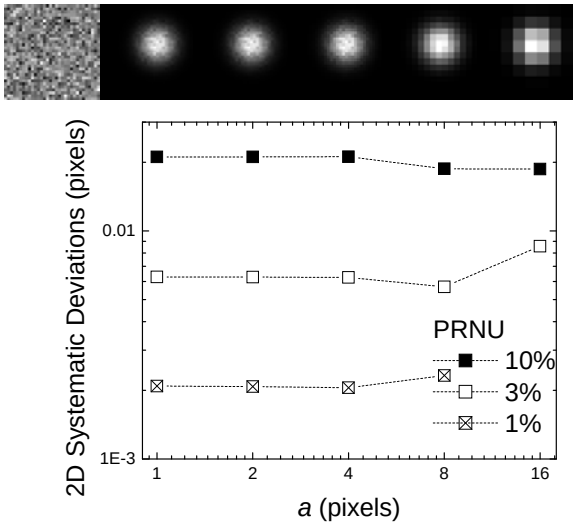

Supplementary Figure 7 Effect of pixelation on PRNU systematic localization errors. Top left panel: PRNU map. Panels from left to right *a*=1,2,4,8,16. Bottom graph, 2D systematic deviations vs. pixel size *a* for 3 levels of PRNU.

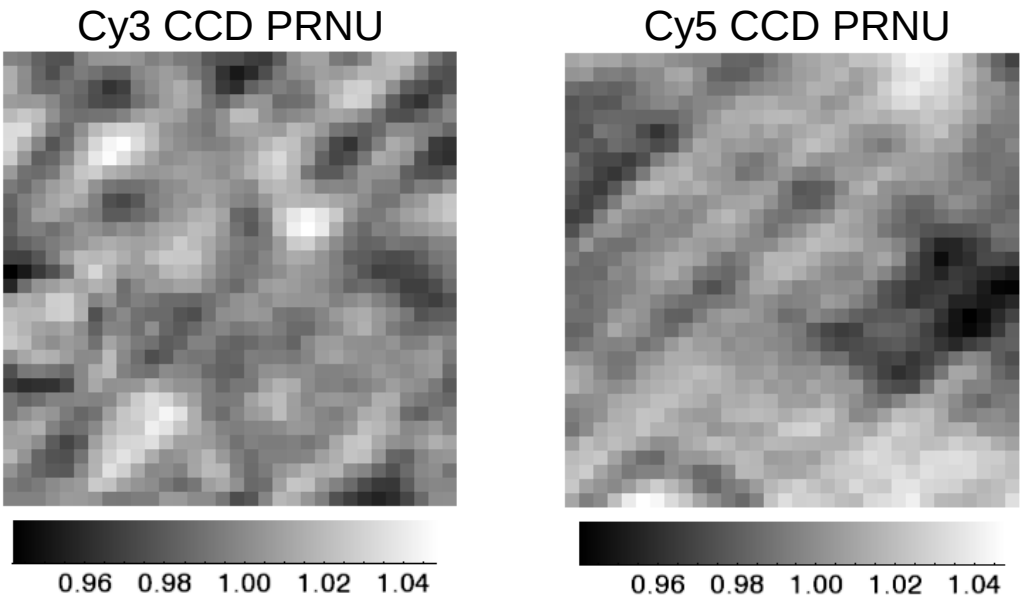

Supplementary Figure 8 Inter-pixel CCD PRNU maps calibrated as explained in the text. The regions are 32×32 pixels and were used for Cy3 and Cy5 imaging during the experiments.

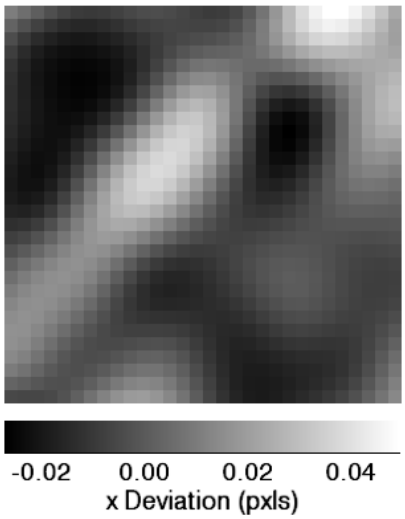
-0.02 0.00 0.02 0.04
x Deviation (pxls)

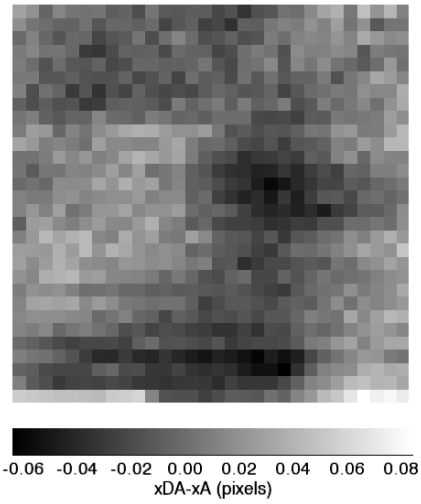
-0.06 -0.04 -0.02 0.00 0.02 0.04 0.06 0.08
xDA-xA (pixels)

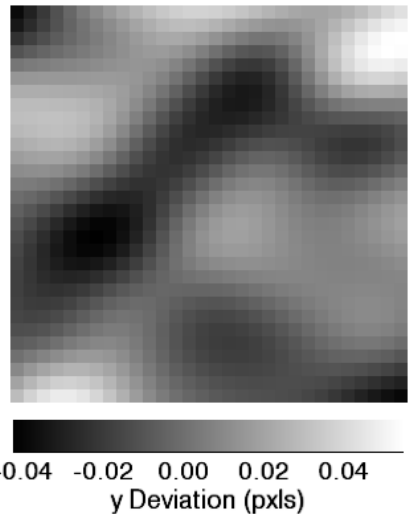
-0.04 -0.02 0.00 0.02 0.04
y Deviation (pxls)

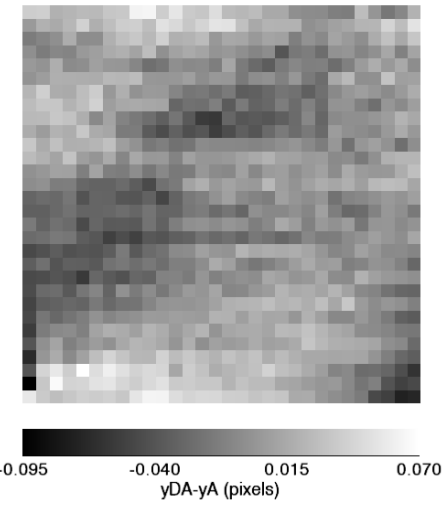
-0.095 -0.040 0.015 0.070
yDA-yA (pixels)

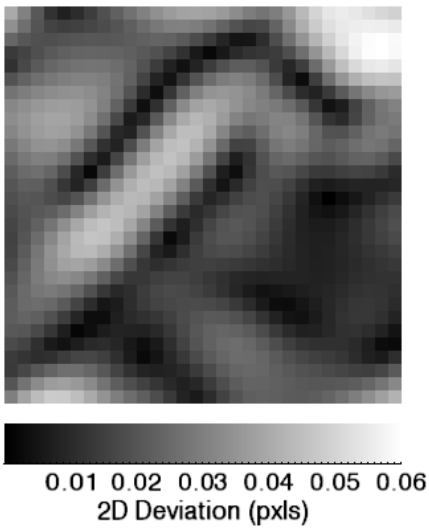
0.01 0.02 0.03 0.04 0.05 0.06
2D Deviation (pxls)

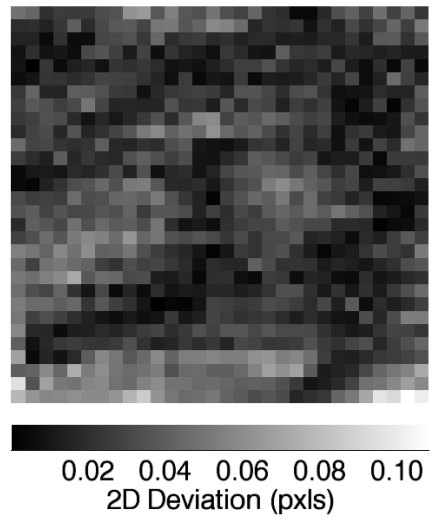
0.02 0.04 0.06 0.08 0.10
2D Deviation (pxls)

Supplementary Figure 9 Comparison between predicted non-linearity due to inter-pixel PRNU (left panels) and experimentally measured non-linearity (right panels). Each panel shows the non-linearity of the mapping function from green to red images. The left panels were calculated based on the PRNU calibration as described in the supplementary text. The right panels were measured with a fluorescent bead that was locked in the vertices of a 30×30 grid with 0.5pxls spacing as described in the main article text.

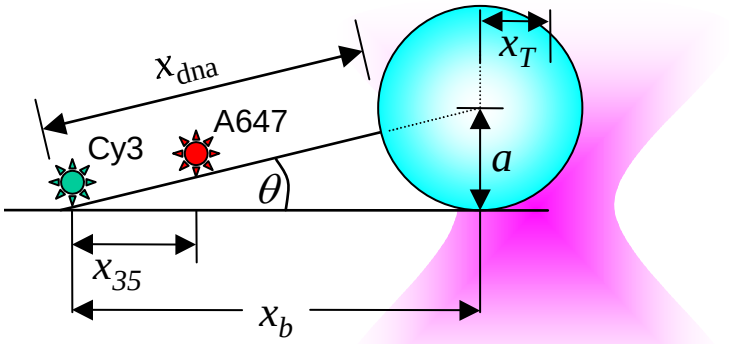

Supplementary Figure 10 Experimental geometry for Cy3-A647 distance measurements on optically manipulated DNA. The geometry is determined from x_b (displacement of the bead in the horizontal direction) and a=250nm. x_T is the displacement from the trap centre and x_{35} is the measured Cy3-Alexa647 distance.

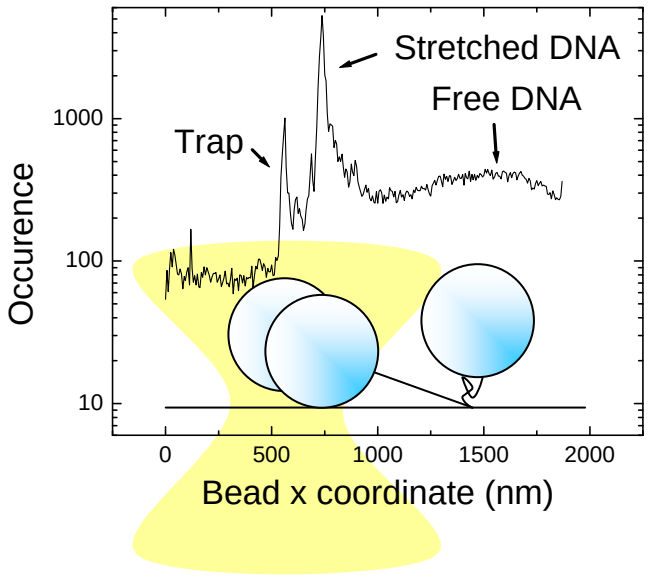

Supplementary Figure 11 Estimation of DNA extension by tracking the bead with CCD1. The trap position is at 550±0.8nm and the DNA attachment point is at 1501±5.5nm. The bead positions for Cy3-Alexa647 spacing of 105bp, 115bp and 125bp are at 738nm, 741nm and 742nm (with ±0.3nm error for all 3) respectively.

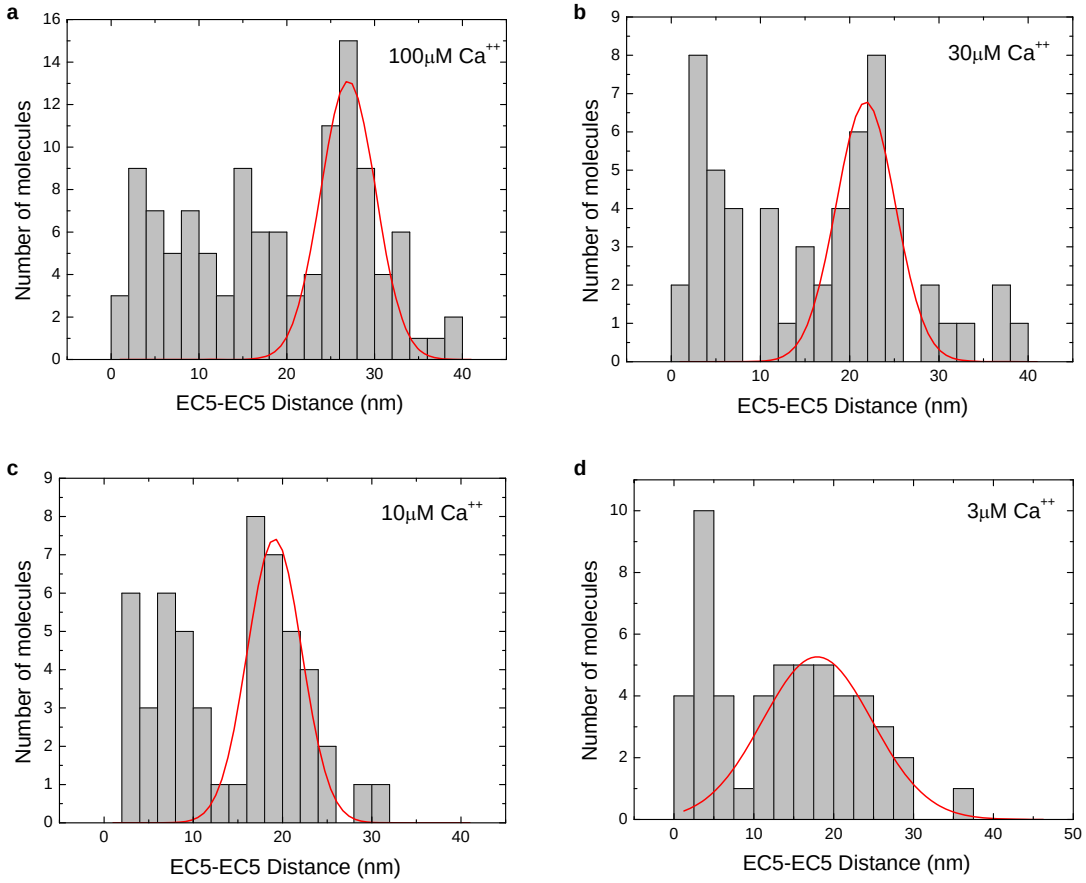

Supplementary Figure 12 [Ca^{++}] Titration Data. (**a-d**) [Ca^{++}] varies between 3μM and 100μM. Solid lines are Gaussian peak fits (see Supplementary Table 3 for fitting parameters).

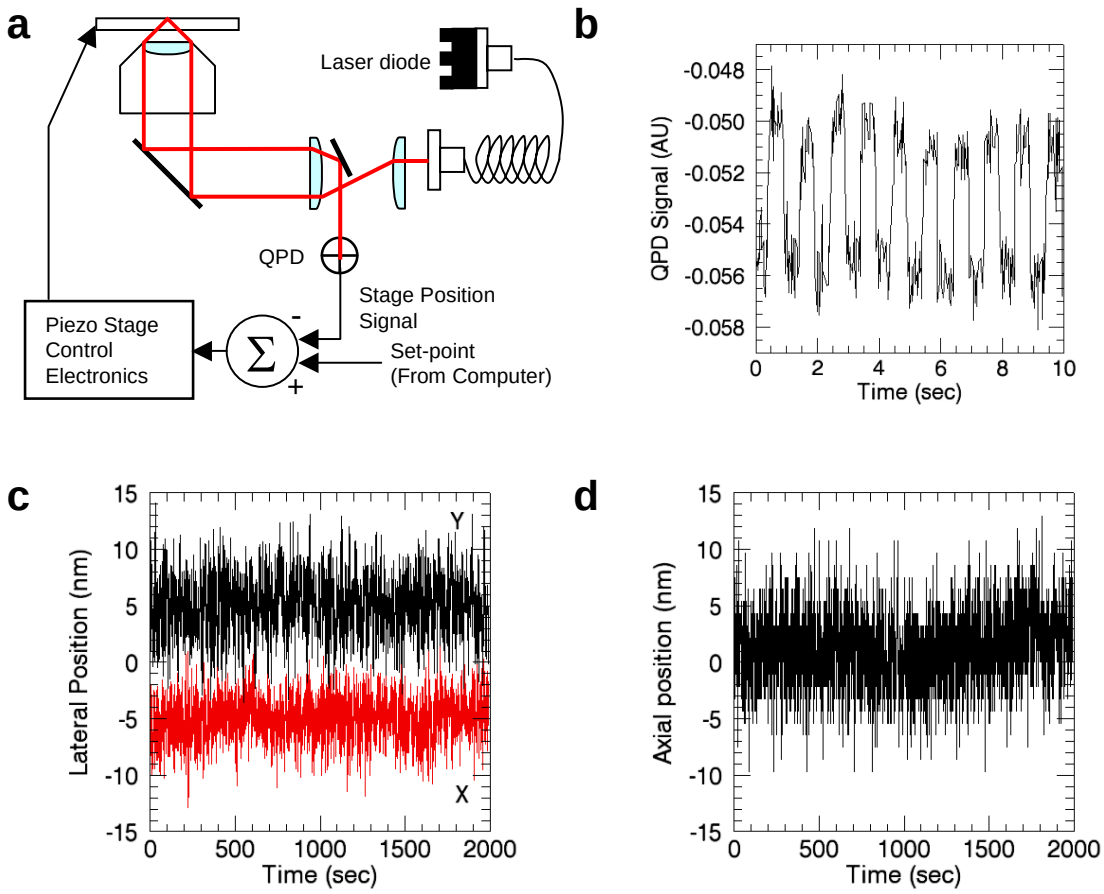

Supplementary Figure 13 3D Active microscope stabilization. (**a**) Alternative setup for axial position stabilization. A laser beam from a temperature-stabilized, fiber-coupled 780nm NIR laser diode (Thorlabs) that undergoes total-internal reflection at the coverslip surface is projected on a Quadrant-photodiode (QPD). The position of the beam on the QPD depends on the coverslip-objective lens separation and generates a signal that drives a digital feedback loop that drives the *z* axis of the 3D piezoelectric stage to adjust the sample axial position. (**b**) QPD signal while the piezo-stage is driven open-loop with a 10nm 1Hz square signal, showing the sensitivity of the setup. (**c-d**) Coordinates of a 0.5μm bead while the CCD image is used to lock the lateral and the QPD signal the axial position of the sample respectively. The r.m.s. stability is 2nm in *xy* and 3nm in *z* over 2000 sec.

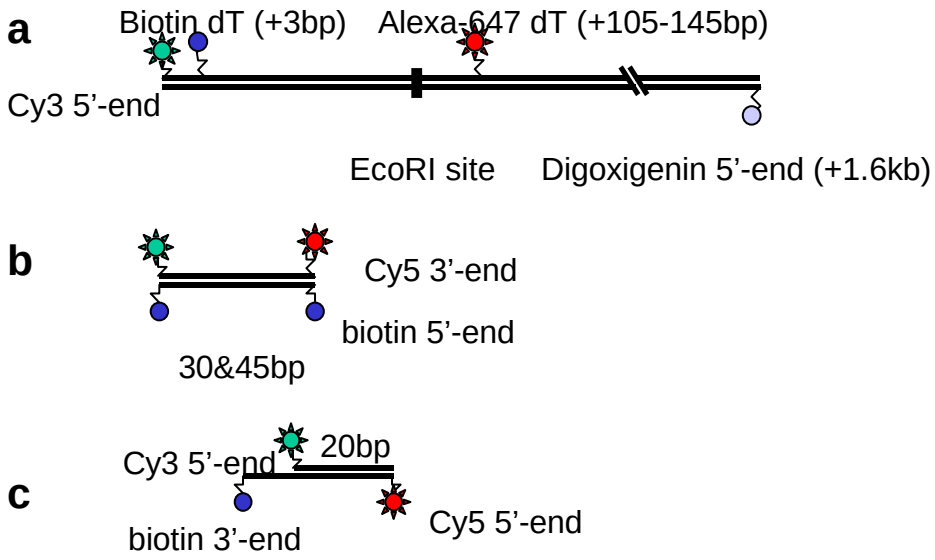

Supplementary Figure 14 Design of DNA constructs. (**a**) DNA constructs that were manipulated with optical tweezers, with Cy3 at one end and internal Alexa647. Total length is ~1.6kb. (**b**) DNA constructs that were immobilized to a streptavidin surface on both ends. Duplex lengths were 30bp and 45bp with Cy3 and Cy5 attached on the two ends. (**c**) DNA construct that was attached only on one end. Cy3-Cy5 separation is 20bp and the attachment to the surface is through a poly-A single-stranded linker.

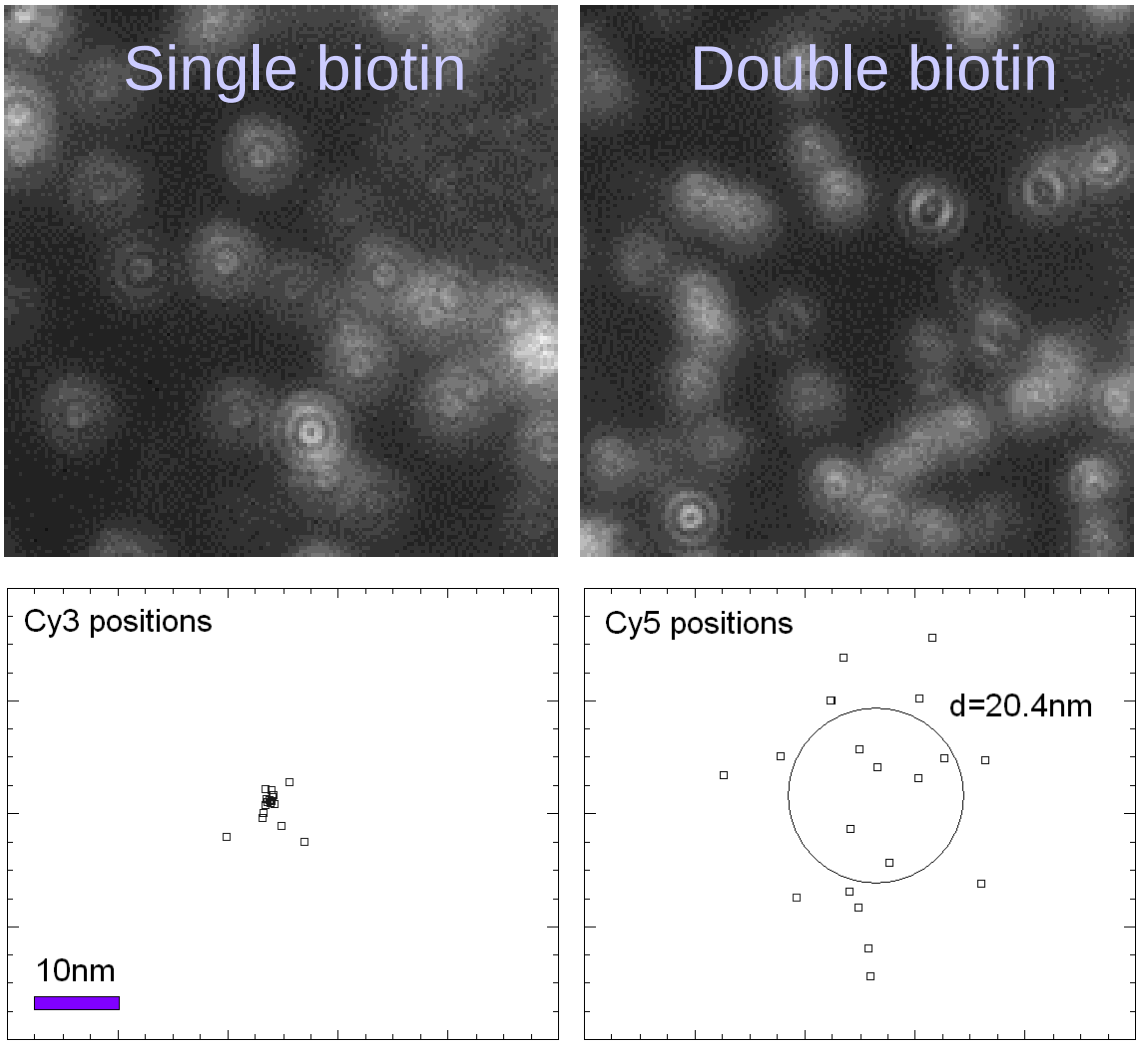

Supplementary Figure 15 Effects of anisotropic fixed-dipole emission. When DNA duplexes with terminally attached Cy3 and Cy5 were immobilized to the surface on both ends, the dye molecules stuck to the DNA [43] or the surface and asymmetric emission patterns were observed. Top left: Out of focus images of Cy3 on the 20bp DNA duplex attached to the surface with a single biotin. The duplex and thus the Cy3 orientation can freely rotate, thus the images look isotropic. Top right: Out of focus images of Cy3 on the 45bp DNA duplex attached to the surface with biotins on both ends. The duplex is immobilized and a large fraction of the Cy3 molecules appear asymmetric due to fixed orientation of their emission dipoles. Such patterns were previously seen [44] and were shown to cause localization errors[45]. Bottom: Errors due to the asymmetry

in the PSF of immobile dipoles. Positions of Cy3 and Cy5 attached to the 30bp duplex, immobilized with biotins of both ends. The Cy3 position was locked (left panel) while the Cy5 positions are expected to fall on a circle with diameter 2×30bp=20.4nm. Deviations from the expected positions are ~5-10nm, consistent with a recent theoretical analysis[46].

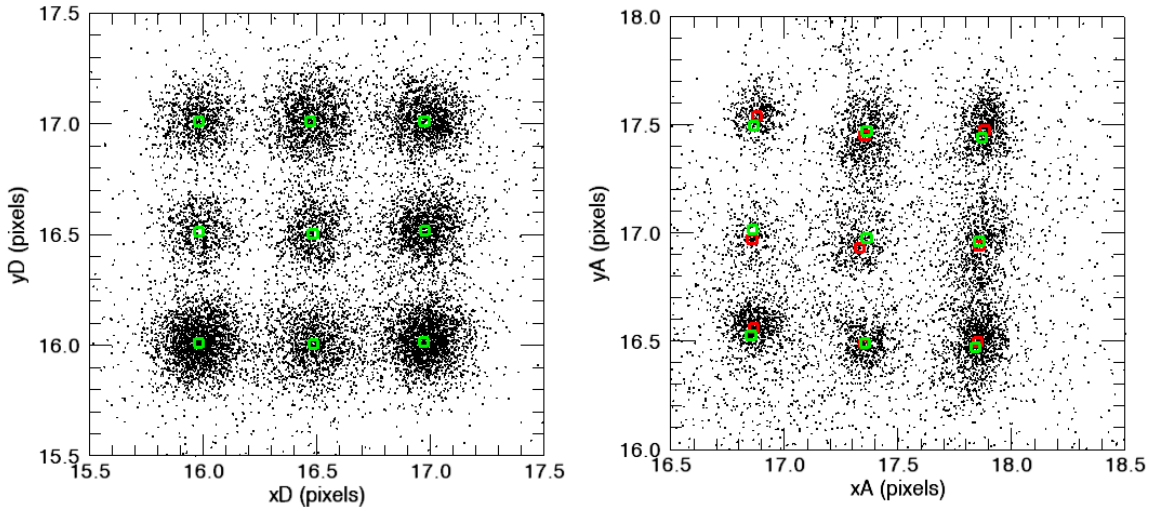

Supplementary Figure 16 Calibration of linear mapping with Cy3 and Cy5 attached to the same 20bp DNA duplex. Left: Cy3 positions (black symbols). Cy3 was locked on the vertices of a 3×3 square grid with 0.5pxls spacing. On each grid point we measured *N*~10 different molecules and took the average position (green symbols). Right: Simultaneous tracking of Cy5 positions (black symbols). Cy5 was attached to the same DNA duplex as Cy3, spaced by 20bp (6.4nm). Red symbols show the average Cy5 positions for each grid point. The green symbols are the positions of the Cy3 mapped to the Cy5 image using the linear mapping transformation as described in the text.

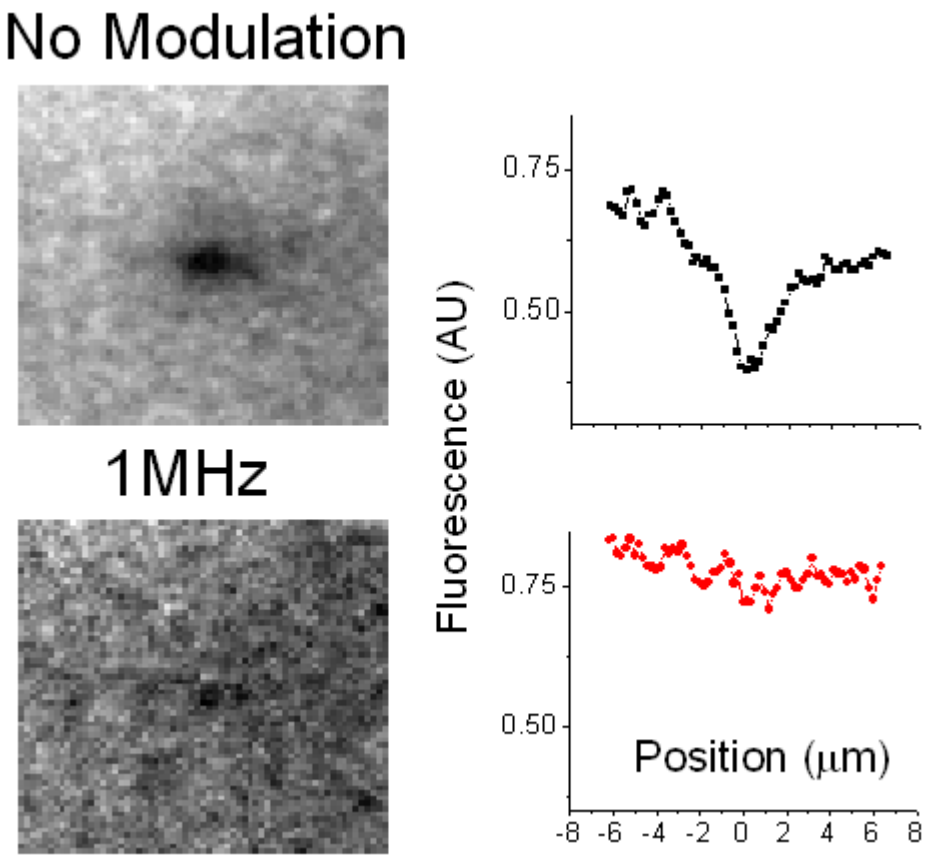

Supplementary Figure 17 Elimination of Cy3 enhanced photo-bleaching. Left panels show the fluorescence intensity profiles of Cy3 molecules covering the surface at high density, while right panels show a line scan of the fluorescence through the trap. When 1064nm and 532nm lasers are on simultaneously the molecules in the middle of the trap show enhanced photo-bleaching, while alternating the two lasers at 1MHz eliminates this effect. The power of the 1064nm laser was 200mW while the 532nm was 10mW and illuminated an area ~50μm in diameter. The exposure for each image is 15sec.

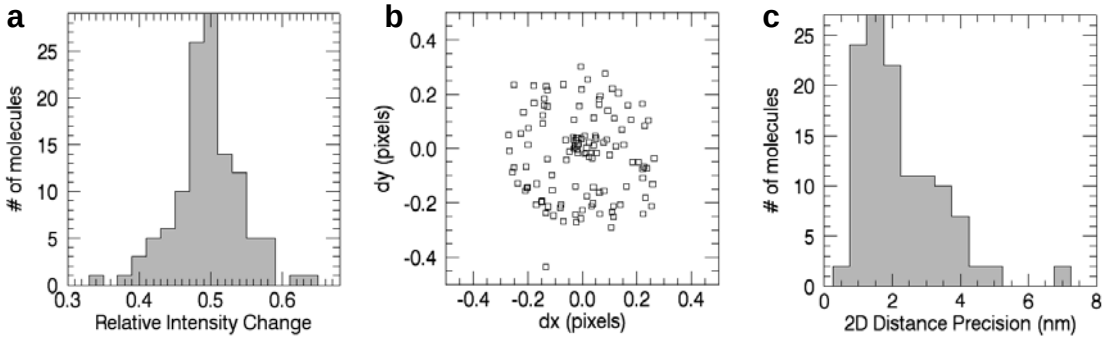

Supplementary Figure 18 EC5-EC5 distance measurements by photobleaching. (**a**) Distribution of the relative intensity change upon photobleaching of the first Alexa647 molecule. (**b**) Displacement points of the image centroid. (**c**) Distribution of the 2D statistical error in the EC5-EC5 distance measurement.

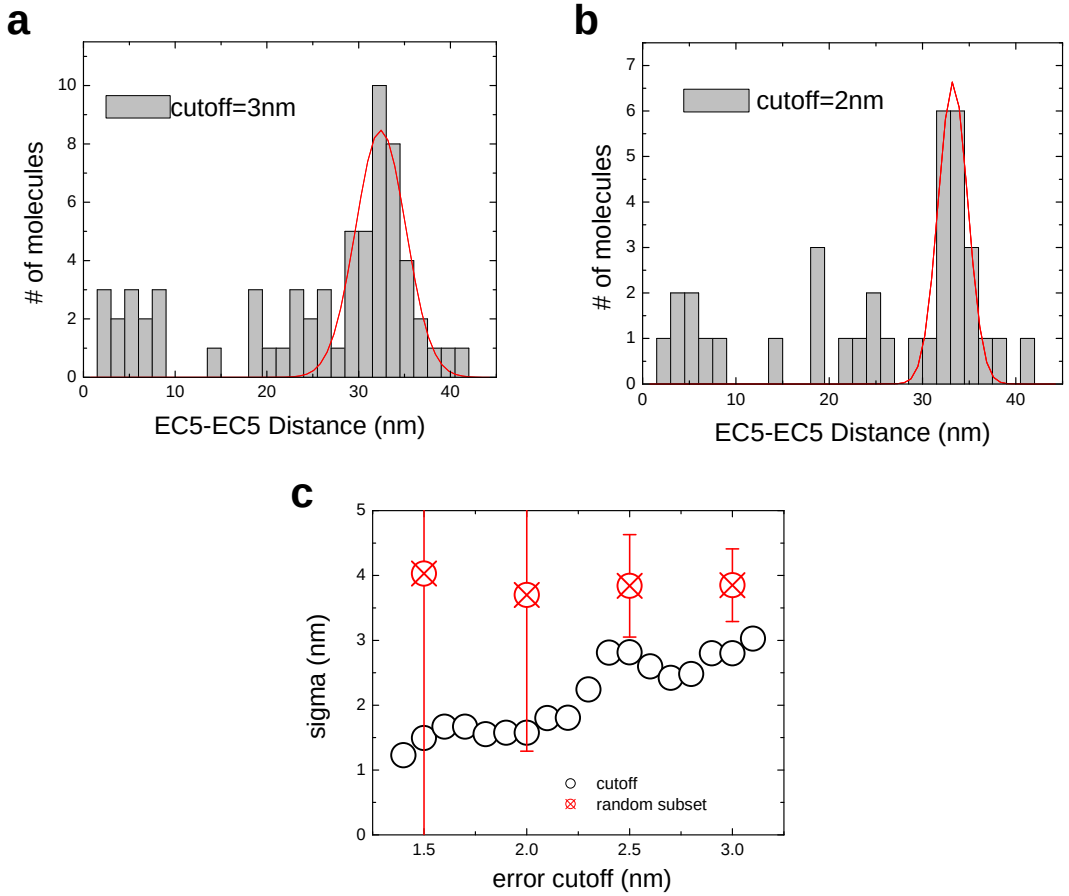

Supplementary Figure 19 Resolution refinement for the main EC5-EC5 distance peak. (**a**) EC5-EC5 distance distribution for all the molecules that had an

expected 2D statistical error better than a cut-off of s_{co}=3nm (see Supplementary Figure 15**c**). Solid line is Gaussian fit with σ=2.7nm, x=32.4nm. (**b**) Similarly for s_{co}=2nm, with σ=1.6nm, x=33.2nm. (**c**) The dependence of the spread σ of the major peak (at 32nm) in the EC5-EC5 distance distribution vs. 2D error cut-off (open circles), showing a continuous decrease in σ with s_{co}, down to $\sigma\approx$1.5nm. The red symbols indicate the absence of such trend in randomly selected sub-sets of size 18%, 41%, 63% and 74% that of the original sample, corresponding to the size of the sub-sets with cut-off 1.5nm, 2nm, 2.5nm and 3nm respectively. Each point is the average σ of N=100 random sub-samples while the error bars indicate the standard deviation in σ.